ACS OMEGA

http://pubs.acs.org/journal/acsodf

Article

Thermally Induced Aragonite−Calcite Transformation in Freshwater Pearl: A Mutual Relation with the Thermal Dehydration of Included Water

Taiga Tone and Nobuyoshi Koga*

Cite This: *ACS Omega* 2021, 6, 13904−13914

Read Online

ACCESS | Metrics & More | Article Recommendations | Supporting Information

ABSTRACT: This study focuses on the relationship between the aragonite−calcite (A−C) transformation and the thermal dehydration of included water in the biomineralized aragonite construction using freshwater pearl. These thermally induced processes occur in the same temperature region. The thermal dehydration of included water was characterized through thermoanalytical investigations as an overlapping of three dehydration steps. Each dehydration step was separated through kinetic deconvolution analysis, and the kinetic parameters were determined. A single-step behavior of the A−C transformation was evidenced using high-temperature X-ray diffractometry and Fourier transform infrared spectrometry for the heat-treated samples. The kinetics of the A−C transformation was analyzed using the conversion curves under isothermal and linear nonisothermal conditions. The A−C transformation occurred in the corresponding temperature region of the thermal dehydration, ranging from the second half of the second dehydration step to the first half of the third dehydration step. Because the thermal dehydration process is constrained by the contracting geometry kinetics, the movement of the thermal dehydration reaction interface can be a trigger for the A−C transformation. In this scheme, the overall kinetics of the A−C transformation in the biomineralized aragonite construction is regulated by a contracting geometry.

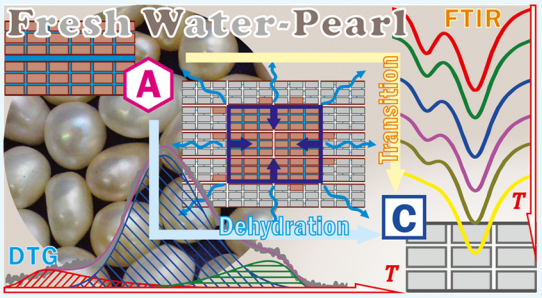

1. INTRODUCTION

Calcium carbonate ($CaCO_3$) is a well-known inorganic raw material and historically used for a variety of applications including architectural materials and pigments.[1,2] There are many sources of $CaCO_3$ available in nature as minerals and those produced through the biomineralization of living organisms. Effective reuse of $CaCO_3$, recovered from waste architectural materials and food processing wastes, is also a focus of materials recycling.[3−11] Therefore, novel potential applications of $CaCO_3$ have been continuously investigated to find additional value and establish cost-effective reuse of the material resource. Recently, the reversible reactions of the thermal decomposition of $CaCO_3$ to form calcium oxide (CaO) and carbon dioxide (CO_2) and the carbonation of CaO to form $CaCO_3$, i.e., $CaCO_3 \rightleftarrows CaO + CO_2$, have attracted considerable attention once again[12−26] The absorption of CO_2 by the carbonation of CaO and recovery of the CaO absorbent by the thermal decomposition of $CaCO_3$ function as a CO_2 looping system to mitigate the greenhouse effect.[12−18] Because of the endothermic thermal decomposition of $CaCO_3$ and exothermic carbonation of CaO, the reversible reactions can be used for the thermal storage of solar energy.[19−26] For these potential applications of the reversible reactions, the physicochemical properties and morphological characteristics of $CaCO_3$ and CaO are recognized as important factors to determine the functionalities.

Two polymorphous crystals of $CaCO_3$ are present in nature, i.e., calcite and aragonite, in addition to the synthetic crystalline phase of vaterite.[27] Naturally available aragonite is the metastable phase, which is transformed into calcite before the thermal decomposition of $CaCO_3$ when it is heated under linear nonisothermal conditions.[28−34] The calcite generated by the thermally induced phase transition of aragonite has some specific morphological characteristics, which are different from the naturally available calcite, and its physicochemical properties and morphological characteristics may depend on the original structural construction of the aragonite and its transformation mechanism to calcite. Thus, a detailed understanding of the aragonite−calcite (A−C) transformation facilitates the control of the physicochemical and morphological characteristics of the as-produced calcite toward the effective use of its functionalities. Thermally induced A−C transformation has been studied from different perspectives. Microscopically, the transformation occurs via nucleation and subsequent growth of the calcite phase.[35−37] From a

Received: March 29, 2021
Accepted: May 7, 2021
Published: May 20, 2021

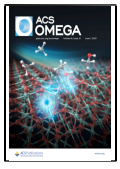

crystallographic viewpoint, the phase transition from aragonite to calcite is explained by reorientation of the CO_3 group to Ca and changes in the Ca atom packing from approximately hexagonal to cubic close-packing, which is followed by the increase in the unit-cell volume.[38,39] The overall kinetic behavior of the A−C transformation has been investigated by focusing on its endothermic behavior using thermoanalytical techniques, including differential thermal analysis (DTA) and differential scanning calorimetry.[28−34,40−45] The nucleation−growth model has also been supported by the kinetic analysis of the thermoanalytical curves,[43−45] even though the reported kinetic parameters are largely distributed. The evolution of water vapor during the A−C transformation has also been revealed through thermoanalytical approaches using thermogravimetry (TG),[28−34] which has been generally observed for the biogenetic aragonite[28−32] and also confirmed for the synthetic aragonite.[29,34] When the A−C transformation and the thermal dehydration of included water occur in the same temperature region, the resulting endothermic behavior should be interpreted by considering the contributions of these two phenomena.[31−33] The evolution of water vapor originated from the thermally induced dehydration of included water in the aragonite construction.[28−34] The thermal dehydration contributes to the increase in the internal pressure of the aragonite construction, and the evolution of water vapor generates diffusion paths such as a micropore in the resulting calcite construction as observed microscopically.[46] Furthermore, the A−C transformation followed by the thermal dehydration of included water occurs at a lower temperature region compared to that of mineral aragonite.[31,46,47] Therefore, elucidation of the interaction between the A−C transformation and the thermal dehydration of included water is necessary to describe the physicogeometrical mechanistic features of the overlapping phenomena.

Our previous study on the A−C transformation of coral aragonite revealed that the accompanying thermal dehydration of included water appears as a partially overlapping multistep process.[48] Thus, the mechanistic correlations of each thermal dehydration step to the A−C transformation may provide additional information to characterize the physicogeometrical mechanisms of the A−C transformation. In this study, biomineralized freshwater pearl (FW-pearl) was used as an aragonite system because fewer contaminants of metal cation other than the calcium ion were expected compared to those mineralized in a seawater environment.[49] The kinetic behaviors of the A−C transformation and the multistep thermal dehydration of included water were separately investigated by following the respective processes using different physicochemical techniques: high-temperature powder X-ray diffractometry (HTXRD) and Fourier transform infrared spectroscopy (FT-IR) for the former and TG for the latter. By comparing the kinetic results, the relationship between the A−C transformation and multistep thermal dehydration in the temperature coordinate was discussed to evaluate the correlations between each thermal dehydration step and the A−C transformation. Further, the physicogeometrical mechanisms of the overall A−C transformation process in the biomineralized construction are discussed in detail by considering the contributions of the thermal dehydration of included water.

2. EXPERIMENTAL SECTION

2.1. Sample and Its Characterization. In this study, FW-pearls produced in China with a diameter size of 7−9 mm were used for experiments (Figure S1). The pearls were crushed and ground using a stainless-steel mortar and pestle. The as-produced pearl powder was sieved using stainless steel sieves with different meshes and an electric shaking apparatus (MVS-1, AS ONE). The powder in the sieved fraction with an aperture size of 90−150 μm was used as the sample (Figure S2). The sample was characterized by powder XRD, FT-IR, and simultaneous TG−DTA measurements. The XRD pattern was recorded using a diffractometer (RINT2200V, Rigaku) by irradiating monochrome Cu Kα (40 kV, 20 mA) and scanning in a 2θ range of 5−60° at a rate of 4° min^{-1} in steps of 0.02°. For the FT-IR spectrum measurement, the sample was diluted with KBr. The FT-IR spectrum was recorded in a spectrometer (FT-IR 8400S, Shimadzu) using the diffuse reflectance method. Figure S3 shows the XRD pattern and FT-IR spectrum of the FW-pearl. The XRD pattern (Figure S3a) is in agreement with that reported for aragonite ($CaCO_3$, orthorhombic, S.G. = Pmcn(62), a = 4.9623, b = 7.9680, c = 5.7439, $\alpha = \beta = \gamma$ = 90.000, ICDD-PDF 00-041-1475).[50,51] The FT-IR spectrum (Figure S3b) shows all of the major IR absorption peaks attributed to aragonite.[52−54] The absorptions attributed to the ν_4 mode of CO_3^{2-} in the aragonite structure are observed at 700 cm^{-1} and 713 cm^{-1}. The IR absorption peaks at 864, 1082, and 1483 cm^{-1} are attributed to the ν_2, ν_1, and ν_3 modes of the CO_3^{2-} vibrations, respectively. The absorption peaks at 1650 and 2600−3600 cm^{-1} correspond to the H−O−H bending and O−H stretching modes of H_2O, respectively, suggesting the presence of H_2O in the aragonite structure as included water, similar to that previously reported for the natural and biomineralized aragonites.[28−34] The atomic constitution of FW-pearl was determined by energy-dispersive X-ray (EDX) spectrometry using an instrument (X-act, Oxford) equipped with a scanning electron microscope (JSM-6510, JEOL). Only Ca, C, and O atoms were detected as the components (Figure S4).

2.2. Tracking of the Thermally Induced Transformations. Approximately 10.0 mg of the sample, weighed into a platinum pan (5 mm in diameter and 2.5 mm in depth), was heated in a TG−DTA instrument (TG8120, Thermoplus 2, Rigaku) from room temperature to 1223 K at a heating rate (β) of 5 K min^{-1} in flowing He gas at a rate of 200 cm^3 min^{-1}. A portion of the outlet gas from the reaction chamber of the TG−DTA instrument was continuously introduced to the quadruple mass spectrometer (M-200QA, Anelva) through a silica capillary tube (0.075 mm inner diameter and 0.7 m in length) heated at 500 K. The mass spectra (MS) of the outlet gas were repeatedly measured in an m/z range from 10 to 50 amu (EMSN: 1.0 mA; SEM: 1.0 kV).

HTXRD measurements were used to track the crystallographic phase changes during heating the sample in the aforementioned XRD instrument by equipping a heating chamber with a programmable temperature controller (PTC-20A, Rigaku). The sample press-fitted to a platinum plate sample holder, ensuring a fine powder bed, was heated in flowing dry N_2 gas at a rate of 100 cm^3 min^{-1} according to two different heating programs. For tracking the crystallographic phase changes in a wide temperature range from 323 to 1123 K, a stepwise isothermal program, composed of 15 min of temperature holding at different temperatures in steps of 50 K

https://doi.org/10.1021/acsomega.1c01683
ACS Omega 2021, 6, 13904−13914

during linear heating at a rate of 2 K min^{-1}, was used to heat the sample, and XRD measurements were performed at each temperature holding section. For tracking the structural phase transition from aragonite to calcite, the sample was initially heated linearly to 703 K at a β of 10 K min^{-1}; subsequently, the sample temperature was maintained at 703 K for 5 h. XRD measurements were repeated 20 times during the isothermal holding section.

The sample of approximately 20 mg, weighed in a platinum pan (5 mm in diameter and 2.5 mm in depth), was subjected to the TG−DTA measurement. TG−DTA curves were recorded using a horizontal thermobalance (TG8121, Thermoplus Evo2, Rigaku) by heating the sample from room temperature to 1223 K at a β of 5 K min^{-1} in flowing dry N_2 gas at a rate of 300 cm^3 min^{-1}. TG−DTA measurements were also carried out in flowing N_2−CO_2 mixed gas (20%-CO_2) at a rate of 300 cm^3 min^{-1} for tracking the water release process observed right before the thermal decomposition of $CaCO_3$ in the TG−DTA measurements under flowing dry N_2 gas. The TG−DTA curves in the flowing N_2−CO_2 mixed gas were recorded at different β values of 1, 2, 3, 5, 7, and 10 K min^{-1}, in which the concentration of CO_2 in the outlet gas from the instrument was continuously monitored using a CO_2 concentration meter (LX-710, IIJIMA).

TG−DTA measurements (β = 5 K min^{-1}) in the flowing N_2−CO_2 mixed gas were stopped at different temperatures in a range of 503−763 K, and the thermally treated samples were recovered after natural cooling to room temperature in the instrument. FT-IR spectra of the thermally treated samples were recorded using the diffuse reflectance method after diluting the samples with KBr (1:10) for determining the mixed ratio of aragonite/calcite. To obtain the calibration curve for determining the aragonite/calcite ratio, FT-IR spectra of standard samples with known aragonite/calcite mixed ratios were also recorded using the same measurement conditions.

3. RESULTS AND DISCUSSION

3.1. Thermal Behavior of FW-Pearl. Figure 1 shows the TG−DTA curves for the powder sample of FW-pearl, along with the MS ion thermograms for m/z = 18 (H_2O^+) and m/z = 44 (CO_2^+) in the gas evolved during heating the sample. The major mass-loss process is observed at a temperature higher than 800 K, followed by the significant endothermic effect. Because the major gaseous product is CO_2, the major mass-loss process is attributed to the thermal decomposition of $CaCO_3$. A detectable mass loss, followed by a slight endothermic effect is observed in a temperature range of 500−800 K, previously to the major mass-loss process. The preliminary mass-loss process is characterized by the evolution of water vapor, i.e., the thermal dehydration of included water.

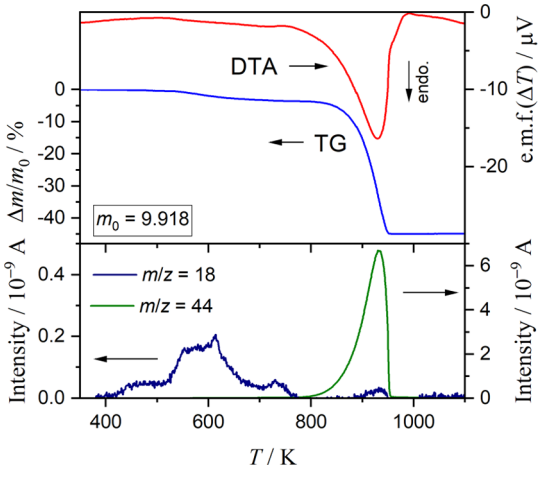

Figure 1. TG−DTA curves for the powdered FW-pearl (m_0 = 9.918 mg) recorded by heating at a β of 5 K min^{-1} in flowing He gas at a rate of 200 cm^3 min^{-1} along with the MS ion thermograms for m/z = 18 (H_2O^+) and m/z = 44 (CO_2^+) in the evolved gas.

Figure 2a shows the changes in the XRD pattern of the sample during the stepwise isothermal heating from 323 to 1123 K in steps of 50 K in flowing dry N_2 gas. The structural phase transition from aragonite to calcite (trigonal, S.G. = R−3c, a = b = 4.9780, c = 17.3540, JCPDS PDF 01-086-2341)[55] (Figure 2b) occurred in the temperature range of 573−773 K by gradual attenuations of aragonite diffraction peaks and compensative growth of those attributed to calcite. The wide temperature range of the A−C transformation observed by the changes in the XRD pattern practically corresponds to that of

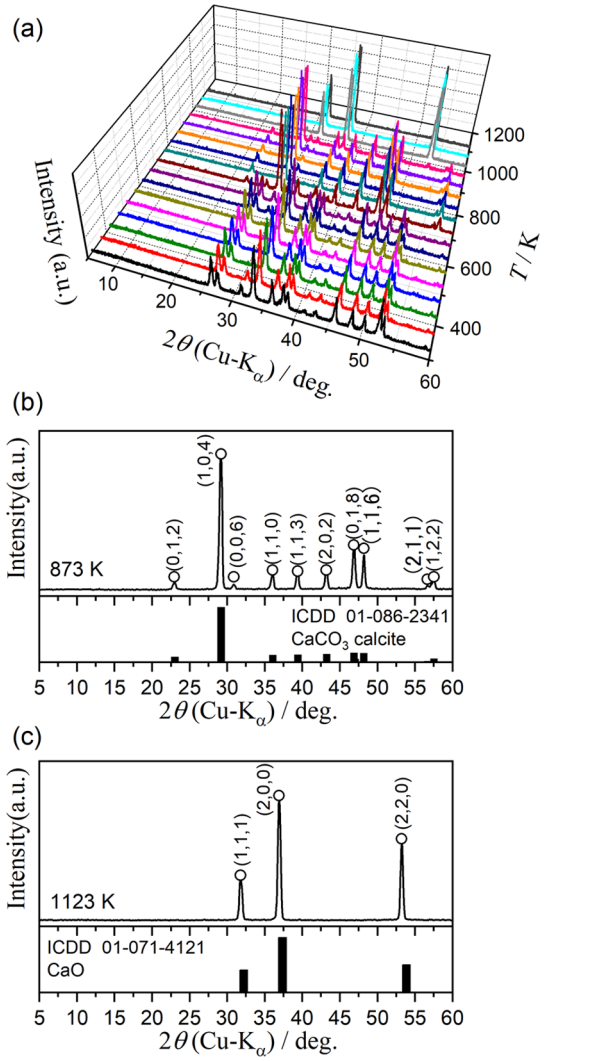

Figure 2. Changes in the XRD pattern of FW-pearl during the stepwise isothermal heating in flowing dry N_2 gas: (a) XRD patterns at different temperatures, (b) XRD pattern at 873 K, and (c) XRD pattern at 1123 K.

https://doi.org/10.1021/acsomega.1c01683
ACS Omega 2021, 6, 13904−13914

the first mass-loss process characterized by the evolution of water vapor in the TG−MS (Figure 1). The as-produced calcite phase decomposes to calcium oxide (Figure 2c) with further heating at temperatures ranging from 873 to 1073 K. The temperature range is approximately 100 K higher than that of the thermal decomposition of calcite observed in the TG−MS. The shift in the temperature range of the thermal decomposition of calcite is explained by the effect of self-generated CO_2 on the reaction under the conditions of the sample press-fitted on the platinum plate for the HTXRD measurement.

Figure 3 shows the change in the XRD pattern of FW-pearl during the isothermal heating at 703 K in flowing dry N_2 gas.

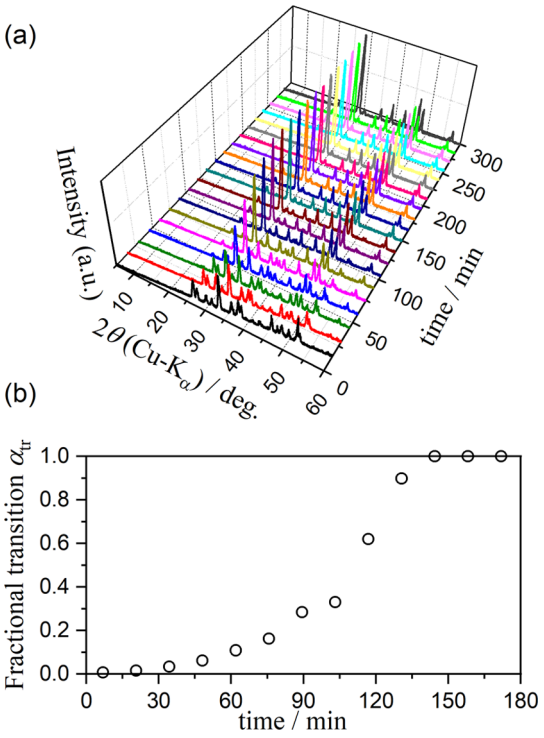

Figure 3. Changes in the XRD pattern of FW-pearl during the isothermal heating at 703 K in flowing dry N_2 gas: (a) XRD patterns at different times and (b) changes in the fractional transition (α_{tr}) from aragonite to calcite, evaluated by the RIR method.

The diffraction peaks of aragonite gradually attenuated as the duration time increased (Figure 3a). In contrast, the intensity of the calcite diffraction peaks increased. The changes in the fractional transition (α_{tr}) from aragonite to calcite as a function of time (Figure 3b), calculated from the XRD patterns using the reference intensity ratio (RIR) method, indicate that the transformation completion at 703 K lasted approximately 150 min. The kinetically controlled feature of the transformation is deduced from the time-dependent transformation behavior at constant temperatures and also from the wide temperature range of the transformation under the stepwise isothermal condition.

Figure 4 shows the comparison of the TG/derivative TG(DTG)−DTA curves for FW-pearl recorded at a β of 5 K min^{-1} in flowing dry N_2 and N_2−CO_2 (20%-CO_2) mixed gases. The first mass-loss process characterized by the evolution of included water in the temperature range corresponding to A−C transformation is not influenced by the atmospheric CO_2. Conversely, the second mass-loss

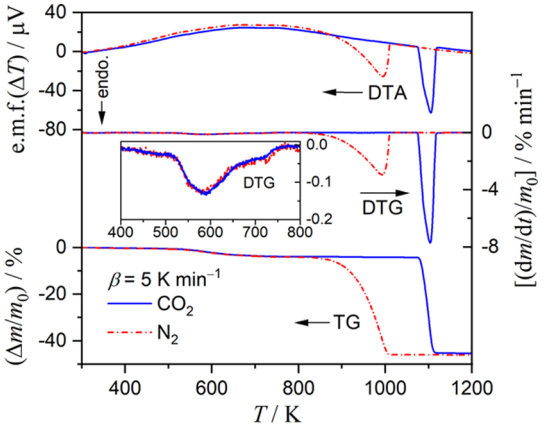

Figure 4. Comparison of TG/DTG−DTA curves for FW-pearl (m_0 = approximately 20.0 mg) recorded at a β of 5 K min^{-1} in flowing dry N_2 and N_2−CO_2 (20%-CO_2) mixed gases.

process of the thermal decomposition of calcite significantly shifts to higher temperatures due to the effect of atmospheric CO_2. These observations demonstrate that the measurement of the thermally induced transformation processes in FW-pearl under atmospheric CO_2 allows monitoring the evolution of water vapor along with the A−C transformation by separating from the subsequent thermal decomposition of calcite.

3.2. Kinetics of Thermal Dehydration of Included Water.

Figure 5 shows the TG−DTG curves recorded at

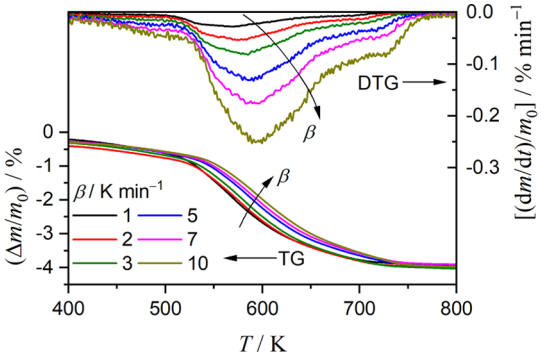

Figure 5. TG−DTG curves for the first mass-loss process of FW-pearl (m_0 = 19.996 ± 0.026 mg) characterized by the evolution of included water recorded at various β values ($1 \le \beta$ (K min^{-1}) ≤ 10) in flowing N_2−CO_2 (20%-CO_2) mixed gases.

different β values in flowing N_2−CO_2 (20%-CO_2) mixed gases by focusing on the temperature range of the thermal dehydration process of included water. The relative mass-loss value for thermal dehydration was 3.98 ± 0.05%. The TG−DTG curves systematically shifted to higher temperatures providing evidence of a kinetically controlled process. The DTG curves during thermal dehydration apparently show three mass-loss peaks partially overlapping. The TG−DTG curves were converted to kinetic curves by calculating the fractional reaction (α) values for the total mass-loss value during the thermal dehydration process (Figure S5).

As a preliminary trial, the overall thermal dehydration process was analyzed kinetically by assuming a single-step reaction using the fundamental kinetic equation that considers the variation of the normalized reaction rate ($d\alpha/dt$) depending on temperature (T) and α values[56−58]

https://doi.org/10.1021/acsomega.1c01683
ACS Omega 2021, 6, 13904−13914

$$\frac{d\alpha}{dt} = A \exp\left(-\frac{E_a}{RT}\right) f(\alpha) \quad (1)$$

where A, E_a, and R are the Arrhenius pre-exponential factor, apparent activation energy, and gas constant, respectively. $f(\alpha)$ is the kinetic model function that describes the change in the $(d\alpha/dt)$ values as a function of α at a constant temperature. By taking logarithms of eq 1, the fundamental kinetic equation is converted to express the isoconversional kinetic relationship, i.e., at a selected α value.[56−58]

$$\ln\left(\frac{d\alpha}{dt}\right) = \ln[Af(\alpha)] - \frac{E_a}{RT} \quad (2)$$

At the selected α value, the data points of $(d\alpha/dt, T)$ extracted from the series of kinetic curves should fulfill the linear correlation between $\ln(d\alpha/dt)$ and T^{-1} under the restriction of a constant ln $[Af(\alpha)]$ value (Friedman plot[59]). The results of the Friedman plots, examined at various α values, are shown in Figure 6. An acceptable linear correlation of the Friedman

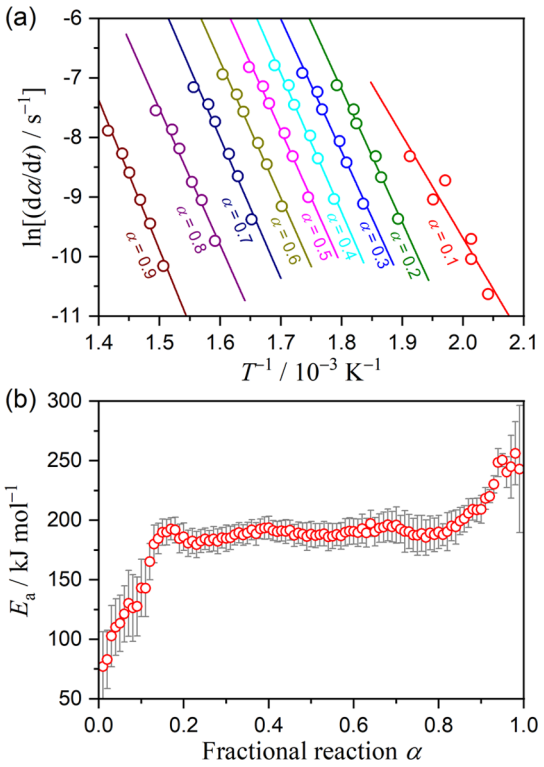

Figure 6. Results of Friedman plots for the thermal dehydration of included water in FW-pearl: (a) Friedman plots at various α and (b) E_a values at various α.

plots was observed at different α values over the course with the correlation coefficient better than −0.98 in the α range of 0.12−0.95 (Figure 6a). However, the E_a value calculated from the slope of the Friedman plots varied during the reaction (Figure 6b). Three distinguishable α ranges exhibiting different E_a variation trends can be identified: (1) the initial E_a increasing range (approximately from 80 to 190 kJ mol^{-1} in $0.01 \le \alpha \le 0.20$), (2) the constant E_a range with an average value of 188.8 ± 3.8 kJ mol^{-1} ($0.20 \le \alpha \le 0.80$), and (3) the final E_a increasing range (approximately from 190 to 250 kJ mol^{-1} in $0.80 \le \alpha \le 0.99$). The observed E_a variation trends also support the overlapping three-step behavior of the thermal dehydration as expected from the shape of the DTG curves at sight (Figure 5). A similar three-step behavior observed for the thermal dehydration of included water was reported for a coral aragonite.[48]

When the component reaction steps during the thermal dehydration of included water are kinetically independent, the overall process is described by a simple cumulative kinetic equation[57,60−62]

$$\frac{d\alpha}{dt} = \sum_{i=1}^{N} c_i A_i \exp\left(-\frac{E_{a,i}}{RT}\right) f_i(\alpha_i) \text{ with } \sum_{i=1}^{N} c_i = 1 \text{ and } \sum_{i=1}^{N} c_i \alpha_i = \alpha \quad (3)$$

where N is the total number of component reaction steps and c is the contribution of each reaction step to the overall process. The subscript i identifies the component reaction step. The kinetic calculation based on eq 3 is the simultaneous determination of all kinetic parameters for all component reaction steps via the nonlinear least-squares analysis to minimize the sum of the squares of the residue between the experimental and calculated data points in the overall kinetic curves (kinetic deconvolution analysis (KDA))[57,60−62]

$$F = \sum_{j=1}^{M} \left[\left(\frac{d\alpha}{dt}\right)_{exp,j} - \left(\frac{d\alpha}{dt}\right)_{cal,j} \right]^2 \quad (4)$$

where M is the total number of data points in a kinetic curve and j identifies the data point. The mathematical procedure always accompanies the possibility to fall in the local minimum, providing the superficial kinetic parameters for all component reaction steps. Setting up the kinetically meaningful initial values at least for several kinetic parameters before the KDA is an approach to increase the reliability of the highly mathematical procedure. In this study, preliminary kinetic analysis for the partially overlapping three-step process ($N = 3$) was performed based on the mathematical deconvolution analysis (MDA) of the overall process using a statistical function.[57,61−64] The MDA provides the initial c_i values from the ratio of the separated peak area of the differential kinetic curves. Furthermore, the initial E_a values for each reaction step are obtained by the conventional isoconversional kinetic analysis. The details of the kinetic analysis based on the MDA are described in the Supporting Information (Section S3: Figures S6−S8 and Table S1).

To achieve the superior curve fitting through the KDA, an empirical kinetic model function $f(\alpha)$, known as Šesták−Berggren model SB(m, n, p),[65−67] was applied to all component reaction steps.

$$f(\alpha) = \alpha^m (1-\alpha)^n [-\ln(1-\alpha)]^p \quad (5)$$

The c_i and $E_{a,i}$ values evaluated through the MDA (Table S1) and SB(0, 1, 0), corresponding to the first-order kinetic model, were introduced into eq 3 as the initial values. Subsequently, the initial A_i values were determined by comparing graphically the positions of the experimental and calculated kinetic curves in the temperature coordinate. Thereafter, all kinetic parameters in eq 3 with eq 5, a total of 18 parameters, were simultaneously optimized through the nonlinear least-squares analysis (eq 4).

Figure 7 shows a typical result of the KDA applied to the thermal dehydration of included water in FW-pearl. Regardless

https://doi.org/10.1021/acsomega.1c01683
ACS Omega 2021, 6, 13904−13914

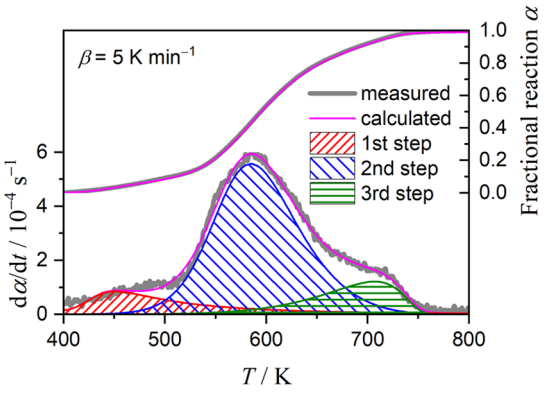

Figure 7. Typical result of the KDA applied to the thermal dehydration of included water in FW-pearl.

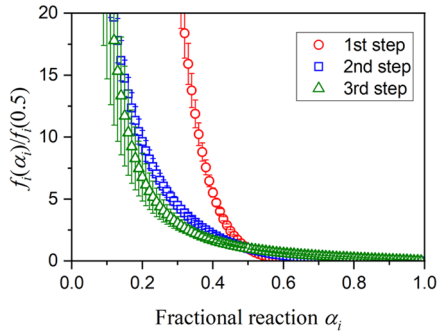

Figure 8. Master plot for each reaction step of the thermal dehydration of included water calculated using the optimized kinetic exponents in SB (m_i, n_i, p_i).

of the kinetic curves at different β values, the statistically significant fit to the overall kinetic curves was achieved, followed by the practically invariant kinetic parameters as listed in Table 1. The largest contribution is observed for the second reaction step, while the contributions of the first and third reaction steps are limited to 10−15%. The increase in the $E_{a,i}$ value followed by the decrease in the A_i value as the reaction step progresses are in agreement with the order of the reaction steps for the reaction temperature. The Arrhenius plots obtained using the optimized kinetic parameters are compared in Figure S9. Using empirical SB(m_i, n_i, p_i) exponents, the master plots for each reaction step were calculated based on the Ozawa's generalized time (θ).[68−75]

$$\frac{d\alpha_i}{d\theta_i} = A_i f_i(\alpha_i) \quad \text{with} \quad \theta_i = \int_0^t \exp\left(-\frac{E_{a,i}}{RT}\right)dt \tag{6}$$

As shown in Figure 8, the master plots exhibit a deceleration process with concaved shapes in all reaction steps, which indicates that the diffusional removal of water molecules through the solid phase is the rate-limiting step.

3.3. Thermally Induced Aragonite−Calcite Transformation. Figure 9 displays the FT-IR spectra of the samples, which were previously heated to different temperatures within the range corresponding to the thermal dehydration of included water at a β of 5 K min^{-1} in flowing N_2−CO_2 mixed gas (20%-CO_2). The characteristic double peaks at 700 and 713 cm^{-1} attributed to the ν_4 mode of CO_3^{2-} in the aragonite structure are maintained until approximately 700 K (Figure 9a). Subsequently, the peak at 700 cm^{-1} attenuates gradually by heating to higher temperatures, and the absorption peak converges with the single peak at 713 cm^{-1} characteristics of the calcite structure. Compared with the temperature range of the thermal dehydration of included water, the A−C transformation occurs in the temperature range between the maximum rates for the second and third thermal dehydration steps. By a quantitative analysis of the

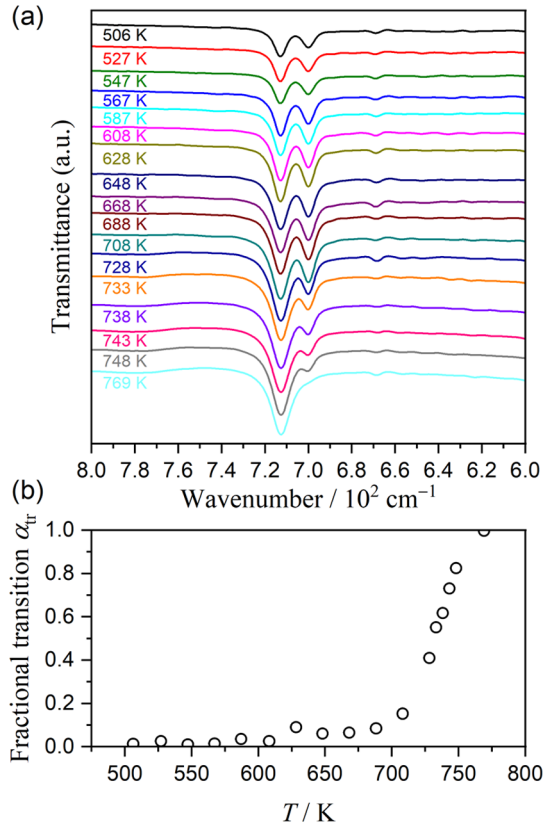

Figure 9. Analysis of FT-IR spectra for the heat-treated sample by heating to different temperatures at a β of 5 K min^{-1} in flowing N_2−CO_2 mixed gases (20%-CO_2) at a rate of 300 cm^3 min^{-1}: (a) changes in the FT-IR spectra for the ν_4 mode of CO_3^{2-} and (b) temperature−fractional transition (α_{tr}) profile from aragonite to calcite determined by the quantitative analysis of the peak area.

absorption peaks using the calibration curve method, the α_{tr} value for the A−C transformation at distinct temperatures was

Table 1. Optimized Kinetic Parameters for the Component Reaction Steps of the Thermal Dehydration of Included Water in FW-Pearl, Averaged Over Different β Values (Determination Coefficient R^2 = 0.9971 ± 0.001)

				$f_i(\alpha_i) = \alpha_i^{m_i}(1-\alpha_i)^{n_i}[-\ln(1-\alpha_i)]^{p_i}$		
i	c_i	$E_{a,i}$/kJ mol^{-1}	A_i/s^{-1}	m_i	n_i	p_i
1	0.14 ± 0.01	160.4 ± 0.8	(1.28 ± 0.03) × 10^{16}	1.53 ± 0.02	8.29 ± 0.43	−1.84 ± 0.03
2	0.73 ± 0.04	193.6 ± 0.5	(5.85 ± 0.03) × 10^{14}	5.67 ± 0.70	0.47 ± 0.02	−6.40 ± 0.64
3	0.13 ± 0.04	219.6 ± 1.2	(1.66 ± 0.01) × 10^{13}	−2.54 ± 0.26	1.09 ± 0.13	0.88 ± 0.06

https://doi.org/10.1021/acsomega.1c01683
ACS Omega 2021, 6, 13904−13914

determined (Figure 9b). From the temperature−α_{tr} profile, the temperature range of the A−C transformation at a β of 5 K min^{-1} was approximately determined to be from 700 to 750 K, and the α_{tr} value systematically increased as the sample temperature increases within the temperature range. The details for the quantitative analysis of the IR absorption peaks are described in the Supporting Information (Section S4: Figures S10−S13 and Tables S2−S4).[53,54,76−80]

The progress of the A−C transformation with time at a constant temperature of 703 K, monitored by XRD measurements (Figure 3), and with temperature at β = 5 K min^{-1}, monitored by FT-IR measurements, were subjected to kinetic analysis as shown in Figure 10. Because the sensitivity and

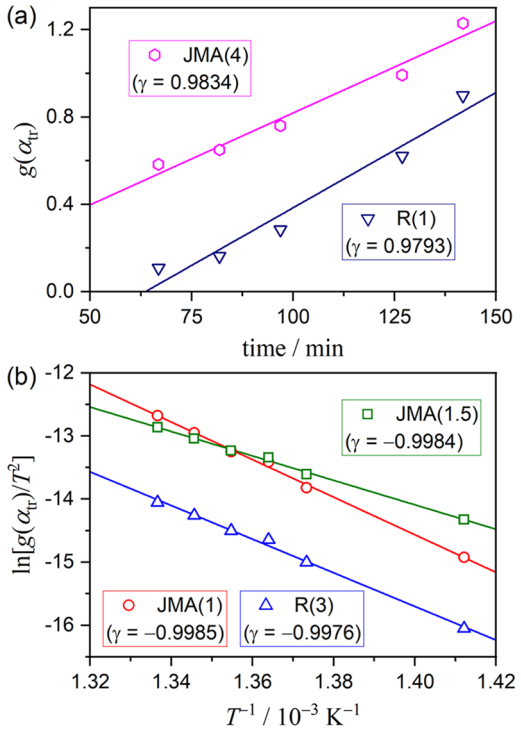

Figure 10. Kinetic plots for the aragonite−calcite transformation: (a) $g(\alpha_{tr})$ versus t plot for the isothermal transformation at T = 703 K tracked using HTXRD (Figure 3) and (b) Coats and Redfern plots[85] for the nonisothermal transformation at β = 5 K min^{-1} tracked using FT-IR (Figure 9).

number of data points of the kinetic data determined using HTXRD and FT-IR are largely limited in comparison with those in TG for the thermal dehydration process, classical integral methods were employed for the kinetic calculation as the only possible method. The changes in α_{tr} with time at a constant temperature can be correlated by the following integral kinetic equation[58]

$$g(\alpha_{tr}) = kt \tag{7}$$

where $g(\alpha_{tr})$ and k are the kinetic model function in the integral form and the rate constant, respectively. By examining $g(\alpha_{tr})$ versus t plots using various $g(\alpha)$ values listed in Table S5, the random nucleation and subsequent growth (Johnson−Mehl−Avrami model; JMA(m))[81−84] and phase boundary-controlled reaction (R(n)) models exhibited the most statistically significant linear correlation between $g(\alpha_{tr})$ versus t with reference to the correlation coefficient (γ) of the linear regression analysis, as shown in Figure 10a. The JMA(4) model explains the constant rate nucleation of calcite in the aragonite matrix and subsequent three-dimensional growth of the nuclei. Conversely, the R(1) model describes the one-dimensional advancement of the transformation interface. Considering the sampling condition of the XRD measurement characterized by the press-fitting on the platinum plate, the physicogeometrical mechanism described by the R(1) model is interpreted by the initiation of the A−C transformation at the top surface of the press-fitted sample and advancement of the transformation interface into the depth. When the thermal dehydration of included water covering the temperature range of the A−C transformation is considered as a possible trigger for the phase transition, the R(1) model is valid as the overall physicogeometrical mechanism because the thermal dehydration characterized by the diffusion-controlled process (Figure 8) occurs with the same geometrical constraint.

The changes in the α_{tr} value with T recorded using the FT-IR measurements for a series of samples with different thermal treatments can be used as the integral kinetic data at a constant β value, which can be kinetically analyzed using the Coats and Redfern (CR) method[85]

$$\ln \frac{g(\alpha_{tr})}{T^2} = \ln\left[\frac{A_{tr}R}{\beta E_{a,tr}}\left(1 - \frac{2RT}{E_{a,tr}}\right)\right] - \frac{E_{a,tr}}{RT} \tag{8}$$

where A_{tr} and $E_{a,tr}$ are the Arrhenius pre-exponential factor and apparent activation energy for the A−C transformation, respectively. By assuming that the logarithmic term on the right-hand side of eq 8 is constant, the plot of ln $[g(\alpha_{tr})/T^2]$ versus the reciprocal temperature represents a linear correlation when an appropriate $g(\alpha)$ is used. The $E_{a,tr}$ and A_{tr} values are then obtained from the slope and intercept of the plot, respectively. As in the kinetic analysis of the isothermal kinetic data, the statistically significant linear correlation of the CR plot is observed when the JAM(m) or R(n) models are adopted (Figure 10b). The kinetic parameters determined by the CR plots are listed in Table 2. The exponent m in JMA(m) representing the optimal linearity of the CR plot was 1.0 or 1.5, which is different from JMA(4) estimated from the HTXRD data under isothermal conditions. Although the physicochemical meaning of the m value is explained by several theoretical interpretations based on the kinetics and geometry of

Table 2. Arrhenius Parameters for the Aragonite−Calcite Transformation Determined by the Coats and Redfern Plot by Adopting Several $g(\alpha)$ Values

function	$g(\alpha_{tr})$	$E_{a,tr}$/kJ mol^{-1}	A_{tr}/s^{-1}	$-\gamma^a$
JMA(1)	$-\ln(1-\alpha_{tr})$	247.5 ± 6.8	(1.47 ± 0.01) × 10^{15}	0.9985
JMA(1.5)	$[-\ln(1-\alpha_{tr})]^{2/3}$	161.0 ± 4.5	(7.23 ± 0.01) × 10^{8}	0.9984
R(3)	$1-(1-\alpha_{tr})^{1/3}$	221.6 ± 7.7	(5.43 ± 0.01) × 10^{12}	0.9976

[a]Correlation coefficient of the linear regression analysis.

https://doi.org/10.1021/acsomega.1c01683
ACS Omega 2021, 6, 13904−13914

successive nucleation and growth,[81−84] the JMA(m) model is fundamentally derived for bulk processes. Therefore, a significant change in the m value depending on the sampling conditions is not expected. The calculated exponent n in the R(n) model determined using the CR plot was 3, which was different from the R(1) estimated from the HTXRD data under isothermal conditions. However, when considering the sample assemblage as the reactant body, the shrinkage dimension of the reaction interface is different depending on the sampling conditions. It is generally accepted that the Arrhenius parameters determined by the CR plot vary depending on $g(\alpha)$ even if statistically significant linear correlations are observed.[86,87] Therefore, the Arrhenius parameters determined by the CR plot can have a certain physical meaning only when the physicogeometrical characteristics are elucidated and a most appropriate kinetic model is selected. Nevertheless, the kinetic triplet, i.e., $E_{a,tr}$, A_{tr}, and $g(\alpha_{tr})$, determined by the CR plot can be used for simulating the kinetic curves, although the applicability of the determined kinetic parameters to the kinetic prediction under different conditions should be further critically examined. Figure 11

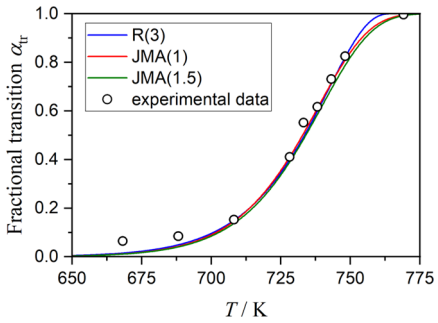

Figure 11. Comparison of the experimental data points with the simulated kinetic curves calculated using the kinetic triplet determined by the Coats and Redfern plots.

compares the experimental kinetic curve (Figure 9b) and the kinetic curves calculated using the kinetic triplet listed in Table 2. The three different sets of the kinetic parameters satisfactorily reproduced the experimental kinetic curve.

3.4. Mutual Relation between the Thermal Dehydration and Aragonite−Calcite Transformation. The evolution of water vapor observed before the thermal decomposition of calcite during linearly heating the FW-pearl was characterized as an overlapping three-step process. Meanwhile, the A−C transformation occurs in the middle of the thermal dehydration of included water at temperatures ranging between the second and third dehydration steps. FW-pearl is defined as the construction of polygonal plates composed of an agglomerate of aragonite crystals, as previously reported for the synthetic aragonite[34] and biomineralized aragonite such as coral aragonite.[48] The included water may be present at the interstices between the aragonite plates and between aragonite crystals. Therefore, the following model for a mutual relationship between the thermal dehydration of included water and A−C transformation was proposed.[48] The first dehydration step is attributed to the included water between the aragonite plates, which enables the subsequent dehydration of the included water between the aragonite crystals in the aragonite plate. Prior to the A−C transformation, an increase in the lattice spacing of the aragonite crystal occurs.[39] Partial dehydration of the included water in the aragonite plate probably provides spaces required for the expansion of the crystal lattice. Consequently, the second dehydration step triggers the A−C transformation. In turn, the A−C transformation enhances the thermal dehydration of the residual included water in the aragonite plates, which appears to be the third dehydration step.

Regardless of the dehydration steps, the movement of the reaction interface controlled by the diffusional removal of water vapor in a contracting geometry scheme is the characteristic kinetic behavior for the thermal dehydration of included water. Therefore, the preparation for the A−C transformation advances with geometrical restrictions of the thermal dehydration. Generally, bulk nucleation and growth, as expressed by the conventional JMA(m) model, are expected for the structural phase transitions. However, the contracting geometry-type model controlled by the constant rate advance of the transformation interface, as expressed by the R(n) model, accurately describes the apparent kinetic behavior of the A−C transformation. The kinetic behaviors of the thermal dehydration process and A−C transformation revealed in this study also support the physicogeometrical model considering the mutual interaction between the thermal dehydration of included water and the A−C transformation in biomineralized aragonites.

4. CONCLUSIONS

As in several biomineralized aragonites, the thermally induced A−C transformation in FW-pearl occurred in the temperature region of approximately 650−750 K by overlapping with the thermal dehydration of included water in the construction. The thermal dehydration of included water was characterized by partially overlapping three dehydration steps. All dehydration steps were kinetically controlled by diffusional removal of water molecules through the construction of aragonite crystals, in which the apparent $E_{a,i}$ values increased as the dehydration step advances, whereas the A_i values exhibited the opposite variation trend. Notably, the second dehydration step accounted for approximately 73% of the mass-loss value for the overall mass-loss value observed during the thermal dehydration of included water. Conversely, the A−C transformation was characterized by a single-step process, exhibiting smooth change in the fractional transition as a function of time and temperature under the isothermal and linear non-isothermal conditions, respectively. By comparing the temperature regions of the multistep thermal dehydration of the included water and the A−C transformation on the temperature axis of linearly increasing temperatures, the temperature region of the A−C transformation was positioned across the second-half of the second dehydration step to the first-half of the third dehydration step. From the time sequence of the overall phenomena, the A−C transformation induced by the second dehydration step and the subsequent third dehydration step induced by the A−C transformation are deduced as the cause and effect relations. In a physicogeometrical viewpoint, the thermal dehydration of included water occurs in a scheme of contracting geometry because the diffusional removal of water vapor is needed. Therefore, the potential sites of the A−C transformation in the construction of the biomineralized aragonite are produced by the movement of the reaction interface of the thermal dehydration of included water (second dehydration step). Although the microscopic mechanism of the A−C transformation is explained by the nucleation and growth mechanism as previously discussed in several studies,

https://doi.org/10.1021/acsomega.1c01683
ACS Omega 2021, 6, 13904−13914

the overall rate behavior of the A−C transformation in the construction of biomineralized aragonite can be controlled by the contracting geometry scheme. This physicogeometrical kinetic model considering the mutual kinetic relationship of the thermal dehydration of included water and the A−C transformation is supported by the kinetic analysis of the A−C transformation, resulting in a possible physicogeometrical constraint described by the phase boundary-controlled model (R(n)).

■ ASSOCIATED CONTENT

Supporting Information

The Supporting Information is available free of charge at https://pubs.acs.org/doi/10.1021/acsomega.1c01683.

Sample characterization (Figures S1−S4); kinetics of the thermal dehydration of the included water (Figure S5); mathematical deconvolution analysis (Figures S6−S9, Table S1); and quantitative analysis of the aragonite and calcite contents using FT-IR spectrum data (Figures S10−S13, Tables S2−S5) (PDF)

■ AUTHOR INFORMATION

Corresponding Author

Nobuyoshi Koga − *Department of Science Education, Division of Educational Sciences, Graduate School of Humanities and Social Sciences, Hiroshima University, Higashi-Hiroshima 739-8524, Japan;* orcid.org/0000-0002-1839-8163; Phone: +81-82-424-7092; Email: nkoga@hiroshima-u.ac.jp

Author

Taiga Tone − *Department of Science Education, Division of Educational Sciences, Graduate School of Humanities and Social Sciences, Hiroshima University, Higashi-Hiroshima 739-8524, Japan*

Complete contact information is available at: https://pubs.acs.org/10.1021/acsomega.1c01683

Notes

The authors declare no competing financial interest.

■ ACKNOWLEDGMENTS

This work was supported by JSPS KAKENHI Grant Numbers 17H00820.

■ REFERENCES

(1) Gettens, R. J.; Fitzhugh, E. W.; Feller, R. L. Calcium Carbonate Whites. *Stud. Conserv.* **1974**, *19*, 157−184.

(2) Tegethoff, F. W. *Calcium Carbonate: From the Cretaceous Period into the 21st Century*; Springer: Basel, 2001.

(3) Janković, B.; Smičiklas, I.; Manić, N.; Mraković, A.; Mandić, M.; Veljović, Đ.; Jović, M. Thermo-Oxidative Evolution and Physico-Chemical Characterization of Seashell Waste for Application in Commercial Sectors. *Thermochim. Acta* **2020**, *686*, No. 178568.

(4) Morris, J. P.; Wang, Y.; Backeljau, T.; Chapelle, G. Biomimetic and Bio-Inspired Uses of Mollusc Shells. *Mar. Genomics* **2016**, *27*, 85−90.

(5) Owuamanam, S.; Cree, D. Progress of Bio-Calcium Carbonate Waste Eggshell and Seashell Fillers in Polymer Composites: A Review. *J. Compos. Sci.* **2020**, *4*, 70.

(6) Cree, D.; Pliya, P. Effect of Elevated Temperature on Eggshell, Eggshell Powder and Eggshell Powder Mortars for Masonry Applications. *J. Build. Eng.* **2019**, *26*, No. 100852.

(7) Lu, J.; Lu, Z.; Li, X.; Xu, H.; Li, X. Recycling of Shell Wastes into Nanosized Calcium Carbonate Powders with Different Phase Compositions. *J. Cleaner Prod.* **2015**, *92*, 223−229.

(8) Katsuyama, Y.; Yamasaki, A.; Iizuka, A.; Fujii, M.; Kumagai, K.; Yanagisawa, Y. Development of a Process for Producing High-Purity Calcium Carbonate ($CaCO_3$) from Waste Cement Using Pressurized CO_2. *Environ. Prog.* **2005**, *24*, 162−170.

(9) Van der Zee, S.; Zeman, F. Production of Carbon Negative Precipitated Calcium Carbonate from Waste Concrete. *Can. J. Chem. Eng.* **2016**, *94*, 2153−2159.

(10) Silva, T. H.; Mesquita-Guimarães, J.; Henriques, B.; Silva, F. S.; Fredel, M. C. The Potential Use of Oyster Shell Waste in New Value-Added by-Product. *Resources* **2019**, *8*, No. 13.

(11) Tsuboi, Y.; Koga, N. Thermal Decomposition of Biomineralized Calcium Carbonate: Correlation between the Thermal Behavior and Structural Characteristics of Avian Eggshell. *ACS Sustainable Chem. Eng.* **2018**, *6*, 5283−5295.

(12) Arcenegui-Troya, J.; Sánchez-Jiménez, P. E.; Perejón, A.; Valverde, J. M.; Chacartegui, R.; Pérez-Maqueda, L. A. Calcium-Looping Performance of Biomineralized $CaCO_3$ for CO_2 Capture and Thermochemical Energy Storage. *Ind. Eng. Chem. Res.* **2020**, *59*, 12924−12933.

(13) Chen, J.; Duan, L.; Sun, Z. Review on the Development of Sorbents for Calcium Looping. *Energy Fuels* **2020**, *34*, 7806−7836.

(14) Nie, L.; Mu, Y.; Jin, J.; Chen, J.; Mi, J. Recent Developments and Consideration Issues in Solid Adsorbents for CO_2 Capture from Flue Gas. *Chin. J. Chem. Eng.* **2018**, *26*, 2303−2317.

(15) Xu, Y.; Ding, H.; Luo, C.; Zheng, Y.; Zhang, Q.; Li, X.; Sun, J.; Zhang, L. Potential Synergy of Chlorine and Potassium and Sodium Elements in Carbonation Enhancement of CaO-Based Sorbents. *ACS Sustainable Chem. Eng.* **2018**, *6*, 11677−11684.

(16) Erans, M.; Manovic, V.; Anthony, E. J. Calcium Looping Sorbents for CO_2 Capture. *Appl. Energy* **2016**, *180*, 722−742.

(17) Nawar, A.; Ghaedi, H.; Ali, M.; Zhao, M.; Iqbal, N.; Khan, R. Recycling Waste-Derived Marble Powder for CO_2 Capture. *Process Saf. Environ. Prot.* **2019**, *132*, 214−225.

(18) Fedunik, H.; Bayon; Donne. Comparative Kinetic Analysis of $CaCO_3$/CaO Reaction System for Energy Storage and Carbon Capture. *Appl. Sci.* **2019**, *9*, 4601.

(19) Edwards, S. E. B.; Materić, V. Calcium Looping in Solar Power Generation Plants. *Sol. Energy* **2012**, *86*, 2494−2503.

(20) Sakellariou, K. G.; Karagiannakis, G.; Criado, Y. A.; Konstandopoulos, A. G. Calcium Oxide Based Materials for Thermochemical Heat Storage in Concentrated Solar Power Plants. *Sol. Energy* **2015**, *122*, 215−230.

(21) Fedunik-Hofman, L.; Bayon, A.; Hinkley, J.; Lipiński, W.; Donne, S. W. Friedman Method Kinetic Analysis of CaO-Based Sorbent for High-Temperature Thermochemical Energy Storage. *Chem. Eng. Sci.* **2019**, *200*, 236−247.

(22) Benitez-Guerrero, M.; Valverde, J. M.; Perejon, A.; Sanchez-Jimenez, P. E.; Perez-Maqueda, L. A. Low-Cost Ca-Based Composites Synthesized by Biotemplate Method for Thermochemical Energy Storage of Concentrated Solar Power. *Appl. Energy* **2018**, *210*, 108−116.

(23) Sánchez Jiménez, P. E.; Perejón, A.; Benítez Guerrero, M.; Valverde, J. M.; Ortiz, C.; Pérez Maqueda, L. A. High-Performance and Low-Cost Macroporous Calcium Oxide Based Materials for Thermochemical Energy Storage in Concentrated Solar Power Plants. *Appl. Energy* **2019**, *235*, 543−552.

(24) Da, Y.; Xuan, Y.; Teng, L.; Zhang, K.; Liu, X.; Ding, Y. Calcium-Based Composites for Direct Solar-Thermal Conversion and Thermochemical Energy Storage. *Chem. Eng. J.* **2020**, *382*, No. 122815.

(25) Sarrión, B.; Perejón, A.; Sánchez-Jiménez, P. E.; Amghar, N.; Chacartegui, R.; Manuel Valverde, J.; Pérez-Maqueda, L. A. Calcination under Low CO_2 Pressure Enhances the Calcium Looping Performance of Limestone for Thermochemical Energy Storage. *Chem. Eng. J.* **2020**, No. 127922.

(26) Sarrión, B.; Perejón, A.; Sánchez-Jiménez, P. E.; Pérez-Maqueda, L. A.; Valverde, J. M. Role of Calcium Looping Conditions on the Performance of Natural and Synthetic Ca-Based Materials for Energy Storage. *J. CO2 Util.* **2018**, *28*, 374−384.
(27) Sarkar, A.; Mahapatra, S. Synthesis of All Crystalline Phases of Anhydrous Calcium Carbonate. *Cryst. Growth Des.* **2010**, *10*, 2129−2135.
(28) Fujinuki, T.; Igarashi, T. On the Water in the Hexacollara. *J. Jpn. Assoc. Mineral., Petrol. Econ. Geol.* **1969**, *62*, 1−17.
(29) Yoshioka, S.; Kitano, Y. Transformation of Aragonite to Calcite through Heating. *Geochem. J.* **1985**, *19*, 245−249.
(30) Baumer, A.; Ganteaume, M.; Bernat, M. Variations De La Teneur En Eau Des Coraux Lors De La Transformation Aragonite → Calcite. *Thermochim. Acta* **1993**, *221*, 255−262.
(31) Passe-Coutrin, N.; N'Guyen, P.; Pelmard, R.; Ouensanga, A.; Bouchon, C. Water Desorption and Aragonite−Calcite Phase Transition in Scleractinian Corals Skeletons. *Thermochim. Acta* **1995**, *265*, 135−140.
(32) Ganteaume, M.; Baumer, A.; Lapraz, D.; Iacconi, P.; Bokilo, J.-E.; Bernat, M.; Zahra, C. La Transformation Aragonite-Calcite Dans Les Coraux Fossiles. Relation Avec La Thermoluminescence. *Thermochim. Acta* **1990**, *170*, 121−137.
(33) Perić, J.; Vučak, M.; Krstulović, R.; Brečević, L.; Kralj, D. Phase Transformation of Calcium Carbonate Polymorphs. *Thermochim. Acta* **1996**, *277*, 175−186.
(34) Koga, N.; Kasahara, D.; Kimura, T. Aragonite Crystal Growth and Solid-State Aragonite−Calcite Transformation: A Physico−Geometrical Relationship Via Thermal Dehydration of Included Water. *Cryst. Growth Des.* **2013**, *13*, 2238−2246.
(35) Milano, S.; Nehrke, G. Microstructures in Relation to Temperature-Induced Aragonite-to-Calcite Transformation in the Marine Gastropod Phorcus Turbinatus. *PLoS One* **2018**, *13*, No. e0204577.
(36) McTugue, J. W., Jr.; Wenk, H.-R. Microstructures and Orientation Relationships in the Dry-State Aragonite−Calcite and Calcite−Lime Phase Transformation. *Am. Mineral.* **1985**, *70*, 1253−1261.
(37) Gomez-Villalba, L. S.; López-Arce, P.; Alvarez de Buergo, M.; Fort, R. Atomic Defects and Their Relationship to Aragonite−Calcite Transformation in Portlandite Nanocrystal Carbonation. *Cryst. Growth Des.* **2012**, *12*, 4844−4852.
(38) Dasgupta, D. R. The Oriented Transformation of Aragonite into Calcite. *Mineral. Mag. J. Mineral. Soc.* **1964**, *33*, 924−928.
(39) Antao, S. M.; Hassan, I. Temperature Dependence of the Structural Parameters in the Transformation of Aragonite to Calcite, as Determined from in Situ Synchrotron Powder X-Ray-Diffraction Data. *Can. Mineral.* **2010**, *48*, 1225−1236.
(40) Perić, J.; Krstulović, R.; Ferić, T.; Vučak, M. The Examination of the Phase Transformation of Aragonite into Calcite by Means of DSC Analysis. *Thermochim. Acta* **1992**, *207*, 245−254.
(41) Wolf, G.; Lerchner, J.; Schmidt, H.; Gamsjäger, H.; Königsberger, E.; Schmidt, P. Thermodynamics of $CaCO_3$ Phase Transitions. *J. Therm. Anal.* **1996**, *46*, 353−359.
(42) Wolf, G.; Gunther, C. Thermophysical Investigations of the Polymorphous Phases of Calcium Carbonate. *J. Therm. Anal. Calorim.* **2001**, *65*, 687−698.
(43) Baitalow, F.; Schmidt, H. G.; Wolf, G. Formal Kinetic Analysis of Processes in the Solid State. *Thermochim. Acta* **1999**, *337*, 111−120.
(44) Davies, P.; Dollimore, D.; Heal, G. R. Polymorph Transition Kinetics by DTA. *J. Therm. Anal.* **1978**, *13*, 473−487.
(45) Topor, N. D.; Tolokonnikova, L. I.; Kadenatsi, B. M. A Study of the Kinetics of the Phase Transition Aragonite → Calcite by Dilatometric Thermal Analysis. *J. Therm. Anal.* **1981**, *20*, 169−174.
(46) Parker, J. E.; Thompson, S. P.; Lennie, A. R.; Potter, J.; Tang, C. C. A Study of the Aragonite-Calcite Transformation Using Raman Spectroscopy, Synchrotron Powder Diffraction and Scanning Electron Microscopy. *CrystEngComm* **2010**, *12*, 1590−1599.
(47) Irigaray, J. L.; Oudadesse, H.; El Fadl, H.; Sauvage, T.; Thomas, G.; Vernay, A. M. Effet De La Temperature Sur La Structure Cristalline D'un Biocorail. *J. Therm. Anal.* **1993**, *39*, 3−14.
(48) Koga, N.; Nishikawa, K. Mutual Relationship between Solid-State Aragonite−Calcite Transformation and Thermal Dehydration of Included Water in Coral Aragonite. *Cryst. Growth Des.* **2014**, *14*, 879−887.
(49) Folk, R. L. The Natural History of Crystalline Calcium Carbonate: Effect of Magnesium Content and Salinity. *J. Sediment. Res.* **1974**, *44*, 40−53.
(50) De Villie, J. P. R. Crystal Structures of Aragonite, Strontianite, and Witherite. *Am. Mineral.* **1971**, *56*, 758−767.
(51) Caspi, E. N.; Pokroy, B.; Lee, P. L.; Quintana, J. P.; Zolotoyabko, E. On the Structure of Aragonite. *Acta Crystallogr., Sect. B: Struct. Sci.* **2005**, *61*, 129−132.
(52) Andersen, F.; Brecevic, L.; et al. Infrared Spectra of Amorphous and Crystalline Calcium Carbonates. *Acta Chem. Scand.* **1991**, *45*, 1018−1024.
(53) Vagenas, N. Quantitative Analysis of Synthetic Calcium Carbonate Polymorphs Using FT-IR Spectroscopy. *Talanta* **2003**, *59*, 831−836.
(54) De Lorenzi Pezzolo, A. The Shell Seeker: What Is the Quantity of Shell in the Lido Di Venezia Sand? A Calibration Drifts Experiment. *J. Chem. Educ.* **2011**, *88*, 1298−1303.
(55) Markgraf, S. A.; Reeder, R. J. High-Temperature Structure Refinements of Calcite and Magnesite. *Am. Mineral.* **1985**, *70*, 590−600.
(56) Koga, N. Ozawa's Kinetic Method for Analyzing Thermoanalytical Curves. *J. Therm. Anal. Calorim.* **2013**, *113*, 1527−1541.
(57) Koga, N. Physico-Geometric Approach to the Kinetics of Overlapping Solid-State Reactions. In *Handbook of Thermal Analysis and Calorimetry*, 2nd ed.; Vyazovkin, S.; Koga, N.; Schick, C., Eds.; Elsevier: Amsterdam, 2018; Vol. *6*, pp 213−251.
(58) Koga, N.; Šesták, J.; Simon, P. Some Fundamental and Historical Aspects of Phenomenological Kinetics in the Solid State Studied by Thermal Analysis. In *Thermal Analysis of Micro, Nano- and Non-Crystalline Materials*, Šesták, J.; Simon, P., Eds.; Springer: 2013; pp 1−28.
(59) Friedman, H. L. Kinetics of Thermal Degradation of Char-Forming Plastics from Thermogravimetry, Application to a Phenolic Plastic. *J. Polym. Sci., Part C: Polym. Symp.* **1964**, *6*, 183−195.
(60) Sánchez-Jiménez, P. E.; Perejón, A.; Criado, J. M.; Diánez, M. J.; Pérez-Maqueda, L. A. Kinetic Model for Thermal Dehydrochlorination of Poly(Vinyl Chloride). *Polymer* **2010**, *51*, 3998−4007.
(61) Koga, N.; Goshi, Y.; Yamada, S.; Pérez-Maqueda, L. A. Kinetic Approach to Partially Overlapped Thermal Decomposition Processes. *J. Therm. Anal. Calorim.* **2013**, *111*, 1463−1474.
(62) Vyazovkin, S.; Burnham, A. K.; Favergeon, L.; Koga, N.; Moukhina, E.; Pérez-Maqueda, L. A.; Sbirrazzuoli, N. Ictac Kinetics Committee Recommendations for Analysis of Multi-Step Kinetics. *Thermochim. Acta* **2020**, *689*, No. 178597.
(63) Perejón, A.; Sánchez-Jiménez, P. E.; Criado, J. M.; Pérez-Maqueda, L. A. Kinetic Analysis of Complex Solid-State Reactions. A New Deconvolution Procedure. *J. Phys. Chem. B* **2011**, *115*, 1780−1791.
(64) Svoboda, R.; Málek, J. Applicability of Fraser−Suzuki Function in Kinetic Analysis of Complex Crystallization Processes. *J. Therm. Anal. Calorim.* **2013**, *111*, 1045−1056.
(65) Šesták, J.; Berggren, G. Study of the Kinetics of the Mechanism of Solid-State Reactions at Increasing Temperatures. *Thermochim. Acta* **1971**, *3*, 1−12.
(66) Šesták, J. Diagnostic Limits of Phenomenological Kinetic Models Introducing the Accommodation Function. *J. Therm. Anal.* **1990**, *36*, 1997−2007.
(67) Šesták, J. Rationale and Fallacy of Thermoanalytical Kinetic Patterns. *J. Therm. Anal. Calorim.* **2012**, *110*, 5−16.
(68) Ozawa, T. Kinetic Analysis of Derivative Curves in Thermal Analysis. *J. Therm. Anal.* **1970**, *2*, 301−324.

https://doi.org/10.1021/acsomega.1c01683
ACS Omega 2021, 6, 13904−13914

(69) Ozawa, T. Applicability of Friedman Plot. *J. Therm. Anal.* **1986**, *31*, 547−551.
(70) Málek, J. The Kinetic Analysis of Non-Isothermal Data. *Thermochim. Acta* **1992**, *200*, 257−269.
(71) Koga, N. Kinetic Analysis of Thermoanalytical Data by Extrapolating to Infinite Temperature. *Thermochim. Acta* **1995**, *258*, 145−159.
(72) Gotor, F. J.; Criado, J. M.; Málek, J.; Koga, N. Kinetic Analysis of Solid-State Reactions: The Universality of Master Plots for Analyzing Isothermal and Nonisothermal Experiments. *J. Phys. Chem. A* **2000**, *104*, 10777−10782.
(73) Criado, J. M.; Perez-Maqueda, L. A.; Gotor, F. J.; Málek, J.; Koga, N. A Unified Theory for the Kinetic Analysis of Solid State Reactions under Any Thermal Pathway. *J. Therm. Anal. Calorim.* **2003**, *72*, 901−906.
(74) Ozawa, T. A New Method of Analyzing Thermogravimetric Data. *Bull. Chem. Soc. Jpn.* **1965**, *38*, 1881−1886.
(75) Ozawa, T. Non-Isothermal Kinetics and Generalized Time. *Thermochim. Acta* **1986**, *100*, 109−118.
(76) Loftus, E.; Rogers, K.; Lee-Thorp, J. A Simple Method to Establish Calcite:Aragonite Ratios in Archaeological Mollusc Shells. *J. Quat. Sci.* **2015**, *30*, 731−735.
(77) De Lorenzi Pezzolo, A. An Exercise on Calibration: Drifts Study of Binary Mixtures of Calcite and Dolomite with Partially Overlapping Spectral Features. *J. Chem. Educ.* **2013**, *90*, 118−122.
(78) Toffolo, M.; Regev, L.; Dubernet, S.; Lefrais, Y.; Boaretto, E. Ftir-Based Crystallinity Assessment of Aragonite−Calcite Mixtures in Archaeological Lime Binders Altered by Diagenesis. *Minerals* **2019**, *9*, 121.
(79) Compere, E. L.; Bates, J. M. Determination of Calcite: Aragonite Ratios in Mollusc Shells by Infrared Spectra1. *Limnol. Oceanogr.* **1973**, *18*, 326−331.
(80) Xyla, A. G.; Koutsoukos, P. G. Quantitative Analysis of Calcium Carbonate Polymorphs by Infrared Spectroscopy. *J. Chem. Soc., Faraday Trans. 1* **1989**, *85*, 3165−3172.
(81) Johnson, W. A.; Mehl, K. F. Reaction Kinetics in Processes of Nucleation and Growth. *Trans. Am. Inst. Min. Metall. Eng.* **1939**, *135*, 416−458.
(82) Avrami, M. Kinetics of Phase Change. I. General Theory. *J. Chem. Phys.* **1939**, *7*, 1103−1112.
(83) Avrami, M. Kinetics of Phase Change. II. Transformation-Time Relations for Random Distribution of Nuclei. *J. Chem. Phys.* **1940**, *8*, 212−223.
(84) Avrami, M. Kinetics of Phase Change. III. Granulation, Phase Change, and Microstructure. *J. Chem. Phys.* **1941**, *9*, 177−184.
(85) Coats, A. W.; Redfern, J. P. Kinetic Parameters from Thermogravimetric Data. *Nature* **1964**, *201*, 68−69.
(86) Vyazovkin, S. V.; Lesnikovich, A. I. Error in Determining Activation Energy Caused by the Wrong Choice of Process Model. *Thermochim. Acta* **1990**, *165*, 11−15.
(87) Koga, N.; Šesták, J.; Málek, J. Distortion of the Arrhenius Parameters by the Inappropriate Kinetic Model Function. *Thermochim. Acta* **1991**, *188*, 333−336.

https://doi.org/10.1021/acsomega.1c01683
ACS Omega 2021, 6, 13904−13914